ADVANCED MATERIALS

Check for updates

Highly Efficient and Stable Solar Cells Based on Crystalline Oriented 2D/3D Hybrid Perovskite

Tong Zhou, Hongtao Lai, Tingting Liu, Di Lu, Xiangjian Wan, Xiaodan Zhang, Yongsheng Liu,* and Yongsheng Chen*

Dedicated to 100th anniversary of Nankai University

Highly efficient and stable 2D/3D hybrid perovskite solar cells using 2-thiophenemethylammonium (ThMA) as the spacer cation are successfully demonstrated. It is found that the incorporation of ThMA spacer cation into 3D perovskite, which forms a 2D/3D hybrid structure, can effectively induce the crystalline growth and orientation, passivate the trap states, and hinder the ion motion, resulting in improved carrier lifetime and reduced recombination losses. The optimized device exhibits a power conversion efficiency (PCE) of 21.49%, combined with a high V_{OC} of 1.16 V and a notable fill factor (FF) of 81%. More importantly, an encapsulated 2D/3D hybrid perovskite device sustains ≈99% of its initial PCE after 1680 h in the ambient atmosphere, whereas the control 3D perovskite device drops to ≈80% of the original performance. Importantly, the device stability under continuous light soaking (100 mW cm^{-2}) is enhanced significantly for 2D/3D perovskite device in comparison with that of the control device. These results reveal excellent photovoltaic properties and intrinsic stabilities of the 2D/3D hybrid perovskites using ThMA as the spacer cation.

Metal halide perovskites solar cells have emerged as one of the most promising photovoltaic technology due to their low processing costs and high power conversion efficiencies (PCEs).[1–3] The high photovoltaic performance is ascribed to their outstanding properties, such as tunable bandgap, low exciton binding energy, long charge carrier lifetime, and low

T. Zhou, H. Lai, T. Liu, D. Lu, Prof. X. Wan, Prof. Y. Liu, Prof. Y. Chen
The Centre of Nanoscale Science and Technology and Key Laboratory of Functional Polymer Materials
Institute of Polymer Chemistry
College of Chemistry
Nankai University
Tianjin 300071, China
E-mail: liuys@nankai.edu.cn; yschen99@nankai.edu.cn
Prof. X. Zhang
Institute of Photoelectronic Thin Film Devices and Technology
Nankai University
Tianjin 300071, China
Prof. X. Wan, Prof. X. Zhang, Prof. Y. Liu, Prof. Y. Chen
Renewable Energy Conversion and Storage Center
Nankai University
Tianjin 300071, China

The ORCID identification number(s) for the author(s) of this article can be found under https://doi.org/10.1002/adma.201901242.

recombination rates.[4–6] The PCEs have been dramatically improved in the past decade and a certified efficiency beyond 23% has already be achieved recently.[7–14] Despite these achievements, however, commercialization of this technology is still restricted by insufficient long-term stability of the devices.[15–17] Therefore, it is necessary to further improve the device stability without sacrificing the efficiency for commercialization of this technology in future.

3D organic–inorganic hybrid perovskite, such as the widely studied perovskite material $CH_3NH_3PbI_3$, suffer from poor light and thermal stability due to the volatility of the methylammonium (MA) organic cation.[15] Thus, formamidinium (FA) based black $FAPbI_3$ (α-phase) has attracted increasing interests due to its broad light absorption range and improved light and thermal stability.[18] More importantly, black $FAPbI_3$ phase can be stabilized by incorporating smaller cations (such as MA, Cs$^+$) into perovskite lattice, leading to efficient perovskite solar cells with improved stability.[19,20] Although tremendous efforts have been devoted to improve photovoltaic performance, the perovskite devices still suffer from poor long-term stability due to the intrinsic instability of 3D perovskite materials.[21]

Recently, Ruddlesden–Popper 2D perovskites have been shown to be more stable than their 3D counterparts due to the improved hydrophobicity and thermostability of the large organic spacer cations, which not only prevents the penetration of water molecules into the perovskite lattice but also plays a role of hindering the ion motion in perovskite film.[22–24] The general formula of Ruddlesden–Popper 2D perovskites is $A_2B_{n-1}M_nX_{3n+1}$, where A is an aliphatic or aromatic alkylammonium cation, B is monovalent cation (such as MA, FA, and Cs$^+$), M is divalent metal cation (such as Pb^{2+} and Sn^{2+}), and X is a halide anion. Note that n value represents the number of corner-sharing $[PbI_6]^{4-}$ octahedral layers and it was used to tune the performance of materials and related photovoltaic cells.[25–27] Recently, Mohite et al. reported a "hot-casting" technique to fabricate highly crystalline 2D perovskite films with the crystalline planes orientated perpendicular to the substrate, which facilitates efficient charge transport between top and bottom electrodes in photovoltaic devices and achieves a high efficiency of 12.5% with improved stability.[23] Since then, the efficiency of 2D perovskite solar cells

ADVANCED
SCIENCE NEWS

www.advancedsciencenews.com

ADVANCED
MATERIALS

www.advmat.de

have been enhanced and an efficiency of over 18% ($n < 5$) has been achieved.[28–33] Despite the significantly improved efficiency and stability, the performances of 2D perovskite solar cells are still relatively poorer in comparison with that of 3D perovskite due to the low charge carrier mobility, relatively large bandgap and hindered charge transport resulted from the insulating organic spacer cations.[24] Consequently, it may be a promising strategy to develop 2D/3D hybrid perovskite materials by combining the advantage of high efficiency of 3D perovskite and high stability of 2D perovskite. However, a search of alternative yet effective organic spacer cations as well as device engineering to fabricate high performance 2D/3D hybrid perovskite solar cells have been experimentally challenging.[34–40]

In this work, we demonstrate highly efficient 2D/3D hybrid perovskite solar cells through incorporation ThMA spacer cations into the FA/MA based 3D perovskite. It is found that the 2D/3D hybrid perovskite exhibits increased grain size and film quality, leading to more balanced charge mobility and long carrier life time. By performing grazing-incidence wide-angle X-ray scattering (GIWAXS) and X-ray diffraction (XRD) experiments, we found that the ThMA spacer cations could induce

the crystalline growth and orientation of 2D/3D perovskite, in which the crystallographic planes of the partly formed 2D $(MA_xFA_{1-x})_{n-1}Pb_nI_{3n+1}^{2-}$ slabs preferentially aligned perpendicular to the substrate, thus facilitate efficient charge transport. The optimized planar devices showed a high open circuit voltage (V_{OC}) of 1.16 V and a very notable fill factor (FF) of 81%, resulting an impressive PCE of 21.49% and a stabilized PCE of 21.1%. More importantly, we found that the stability of 2D/3D hybrid perovskite solar cells was improved significantly. Encapsulated devices sustain over 99% of their original efficiency after stored 1680 h in air. Importantly, the devices stability was enhanced significantly for 2D/3D perovskite device in comparison with control device under continuous light soaking (100 mW cm^{-2}). Our results further suggest that the incorporation of a small fraction of ThMA organic spacer cations into 3D perovskite lattice forming 2D/3D hybrid materials is an efficient strategy to combine the advantage of 2D and 3D perovskite toward efficient and stable solar cells.

Figure 1a shows a schematic illustration of the planar heterojunction solar cell with architecture of glass/indium tin oxide (ITO)/SnO$_2$/perovskite/2,2′7,7′-tetrakis-(N,N-di-p-methoxyphenyl
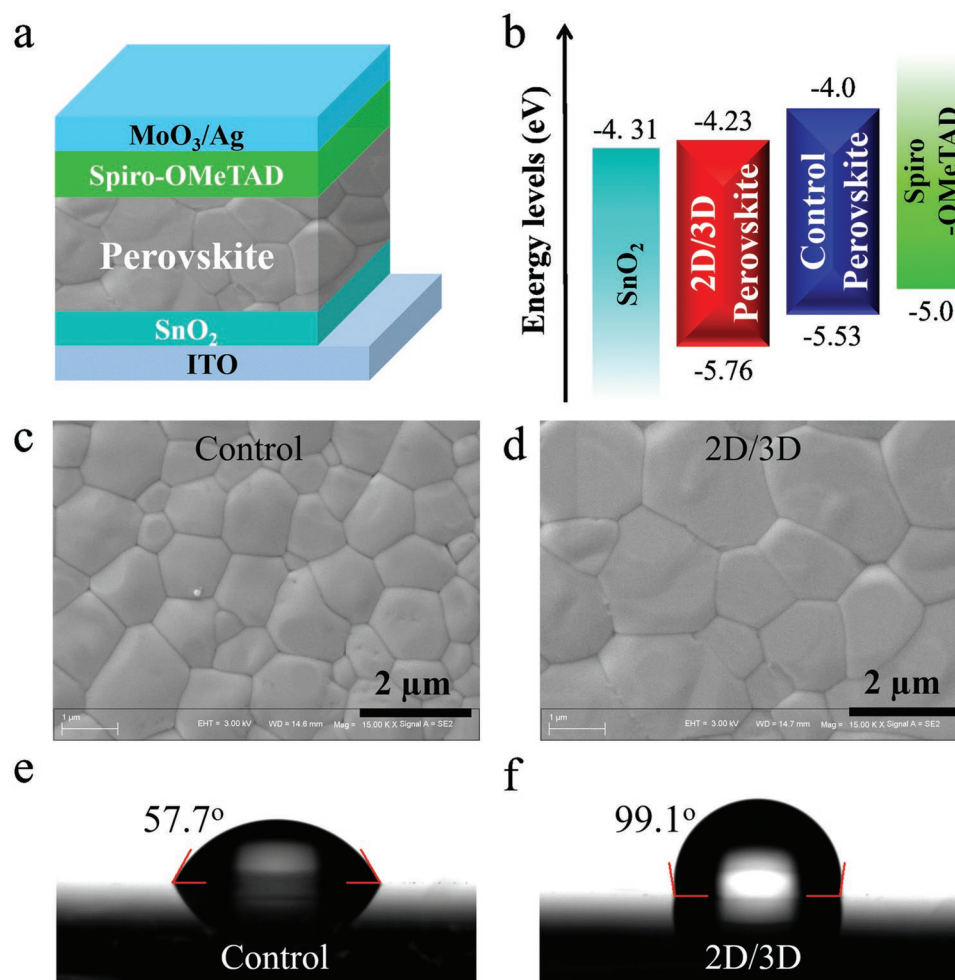
Figure 1. a) Device structure of planar perovskite solar cells. b) Energy levels of optimized 2D/3D hybrid perovskite, control 3D perovskite, and charge transport materials used in the devices. c) Top-view SEM images of the control 3D perovskite film on the glass/SnO$_2$ substrate. d) Top-view SEM images of the 2D/3D perovskite film on the glass/SnO$_2$ substrate. e,f) Images of water droplet contact angles on surfaces of the control (e) and the 2D/3D perovskite (f) films with a loading time of 5 s.

amine)-9,9′-spirobifluorene (spiro-MeOTAD)/MoO$_3$/Ag. The cross-section scanning electron microscopic (SEM) images of the devices are shown in Figure S1 (Supporting Information). The valence band maximum (VBM) of the optimized 2D/3D perovskite and control 3D perovskite were determined by ultraviolet photoelectron spectroscopy (UPS) (Figure S2; Table S1, Supporting Information), and the conduction band maximum (CBM) were estimated by subtracting the VBM from the optical bandgap. Note that optimized ThMAI content in the 2D/3D perovskite is 8%, which is based on the total weight of formamidinium iodide (FAI) and methylammonium iodide (MAI) in the precursor solution unless otherwise stated. The changed VBM and CBM for ThMAI incorporated perovskite suggested the formation of 2D/3D hybrid perovskite,[41] which is consistent with the results discussed below. As shown in Figure 1b, the energy levels of the 2D/3D perovskite matched well with charge transporting materials, such as SnO$_2$ and Spiro-OMeTAD, indicating its potential as a photoactive material in high performance solar cells. The Fourier transform infrared (FTIR) spectra of ThMAI, (ThMA)$_2$PbI$_4$, control and 2D/3D perovskite films are shown in Figure S3 (Supporting Information). The following spectral features and peak positions were observed: N–H stretching peak at 3408 cm^{-1} for 3D perovskite and 3398 cm^{-1} for 2D/3D hybrid perovskite, and C−H

(C=C−H in thiophene) stretching peak at 3161 cm^{-1} for ThMAI, (ThMA)$_2$PbI$_4$ and 2D/3D perovskite. We attribute this spectral change to the formation of 2D/3D perovskite. Figure 1c,d shows top-view SEM images of control and 2D/3D perovskite films. It can be seen that the control perovskite film has a relatively small grain size and the grain size was dramatically increased for 2D/3D hybrid films. The increased grain size may be ascribed to the π–π interaction of thiophene rings resulting from the ThMA spacer cations, which could connect the 3D perovskite effectively.[30] As the hydrophobicity of perovskite films plays an important role for their air stability, the water wetting behavior of perovskite films were investigated. As shown in Figure 1e,f, the ThMA spacer cations incorporated 2D/3D hybrid perovskite film shows contact angle of 99.1°, which is much larger than that (57.7°) of control 3D perovskite film, indicating that the 2D/3D perovskite is more hydrophobic. Figure S4 (Supporting Information) shows the contact angles of water droplet on control and 2D/3D perovskite films with different loading time. When the water loading time increased to 6 min, the 2D/3D film still maintained a large contact angle of 79.6°, which is much larger than that (30.9°) of control film. The results suggest that the 2D/3D perovskite with ThMA spacer cations could be more efficient to protect the perovskite film from moisture.
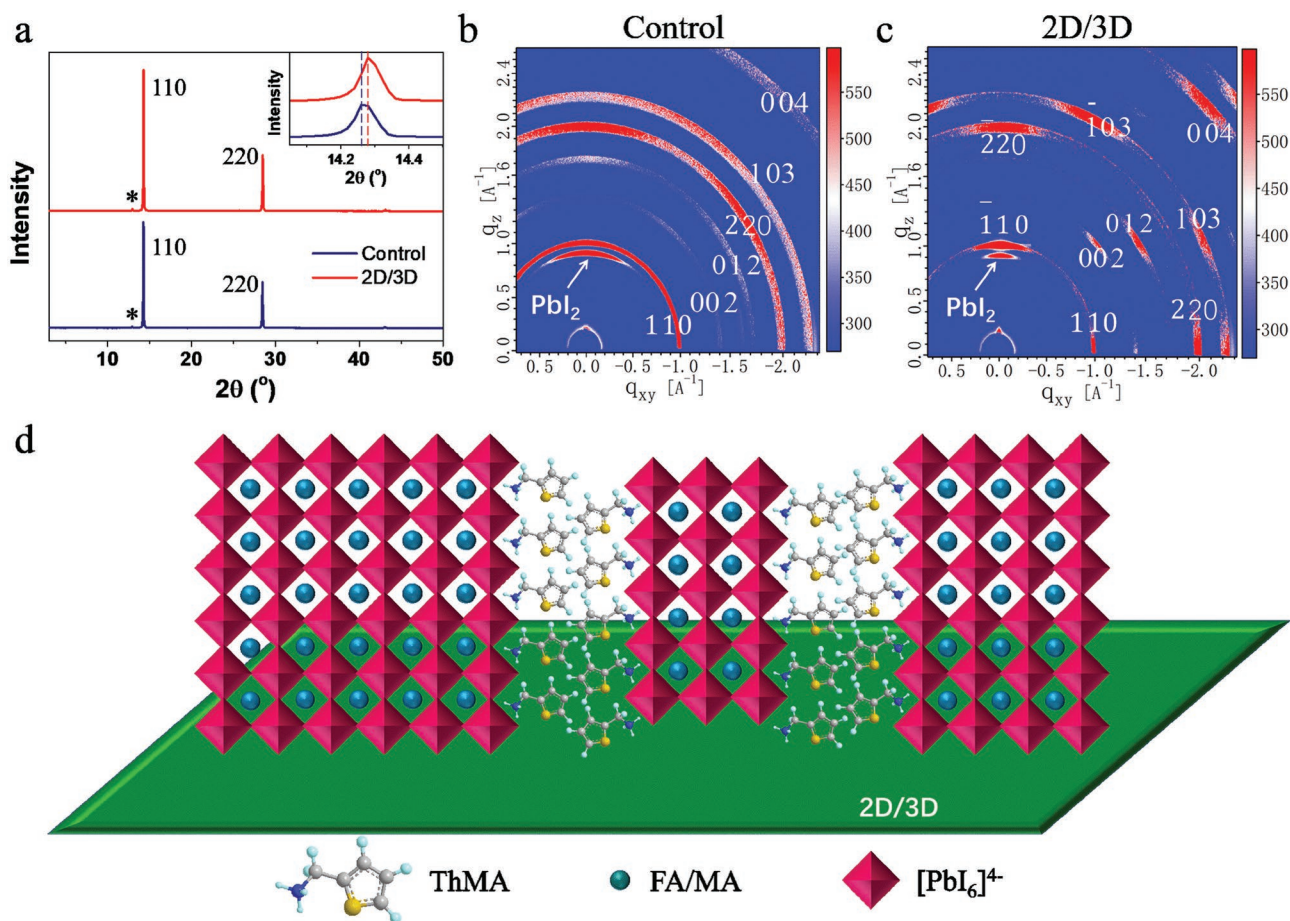
Figure 2. a) XRD patterns of control and 2D/3D perovskite films. Inset is the magnified graph of the main perovskite peaks between 14.1° and 14.5°. Asterisks denote the major reflections from PbI2. b) GIWAXS of control 3D perovskite film. c) GIWAXS of 2D/3D perovskite film. d) Schematic illustration of the proposed 2D/3D perovskite structure, where the organic layer randomly inserted into the 3D perovskite and oriented perpendicular to the substrates.

**ADVANCED
SCIENCE NEWS**

www.advancedsciencenews.com

**ADVANCED
MATERIALS**

www.advmat.de

The XRD patterns (**Figure 2**a) show clear and sharp characteristic perovskite peaks with a preferential (110) and (202) orientation for 2D/3D perovskite films. The main perovskite peak around 14° is slightly shifted to a higher angle for 2D/3D perovskite, indicating that ThMA cations have been inserted into the MAI and FAI based control 3D perovskite and thus form 2D/3D hybrid perovskite film. The formed 2D/3D structure was further verified using X-ray photoelectron spectroscopy (XPS) (Figure S5, Supporting Information), which reveal that the peaks, including Pb 4f, I 3d, and N 1s, shifted to higher binding energy as compared to that of control film. It thus confirms the ThMA cations have been inserted into the perovskite crystal lattice and form 2D/3D hybrid structure. As shown in Figure 2a, there is no new peak emerged at the small diffraction angle ($2\theta < 12°$) for ThMA incorporated perovskite, validating preferential crystalline orientation in 2D/3D perovskite, which is consistent with the GIWAX data below.[30,42] The 2D/3D film exhibits a higher diffraction peak intensity and a smaller the full width at half maximum (FWHM) for the main (110) peak, suggesting a better crystallinity, which agrees well with the larger grain size observed in SEM images. Note that both the control and 2D/3D perovskite films contain residual PbI_2 with a very weak peak around 12.9°, which was also observed in the GIWAX data shown in Figure 2b,c. A small quantity of residual PbI_2 mainly plays the role of grain boundary passivation and hole-blocking effect, leading to improved photovoltaic performance.[43–45]

We conducted GIWAXS analysis to probe the crystalline orientation of the 2D/3D perovskite film and to gain deeper insights into the crystallization process. Figure 2b,c depicts the GIWAXS data obtained from control and 2D/3D perovskite films. The control film exhibits the key features of the 3D

perovskite structure, represented by the broad Debye–Scherrer rings. The corresponding diffraction rings of the control film show relatively homogeneous azimuthal intensity distribution, indicating an isotropic orientation distribution of the crystallites.[10] In contrast, the ThMAI-incorporated 2D/3D perovskite film exhibits a higher diffraction intensity with sharp, sporadic Bragg spots, which suggests partial reorientation of crystallites upon formation of the 2D/3D hybrid layer.[23] Note that no (0k0) diffractions were observed in both film XRD and GIWAXS data, indicating that highly oriented crystal grains with vertical growth of inorganic corner-sharing $[PbI_6]^{4-}$ sheets on the substrate.[23,30] Considering the high orientation of the first feature, we conclude that this increase in crystal orientation can be linked to the incorporation of large organic cation, ThMAI, which partially inserted in the 3D perovskite film and form a 2D layer aligned perpendicular to the substrate, as illustrated in Figure 2d. ThMA cations could form extended organic sheets due to π-stacking of the thiophene-rings and hydrogen-bonding interactions between the NH_3^+ group with the neighboring $[PbI_6]^{4-}$ octahedra layer, respectively.[46,47] It can be speculated that the incorporation of ThMA spacer cation, which is much larger than MA or FA and is hard to migrate, may lead to reduced ionic (such as MA, I^-) migration and improved hydrophobic properties of the perovskite film, resulting increased stability under ambient conditions as discussed below.

The detailed statistical photovoltaic performance parameters for control and 2D/3D perovskite devices are shown in Figure S6 (Supporting Information). The performance of the device increased first for films treated with different content of ThMAI in the precursor solution and decreased when using excess ThMAI, with the best performance attained when 8% ThMAI was used. **Figure 3**a shows the J–V characteristics of control
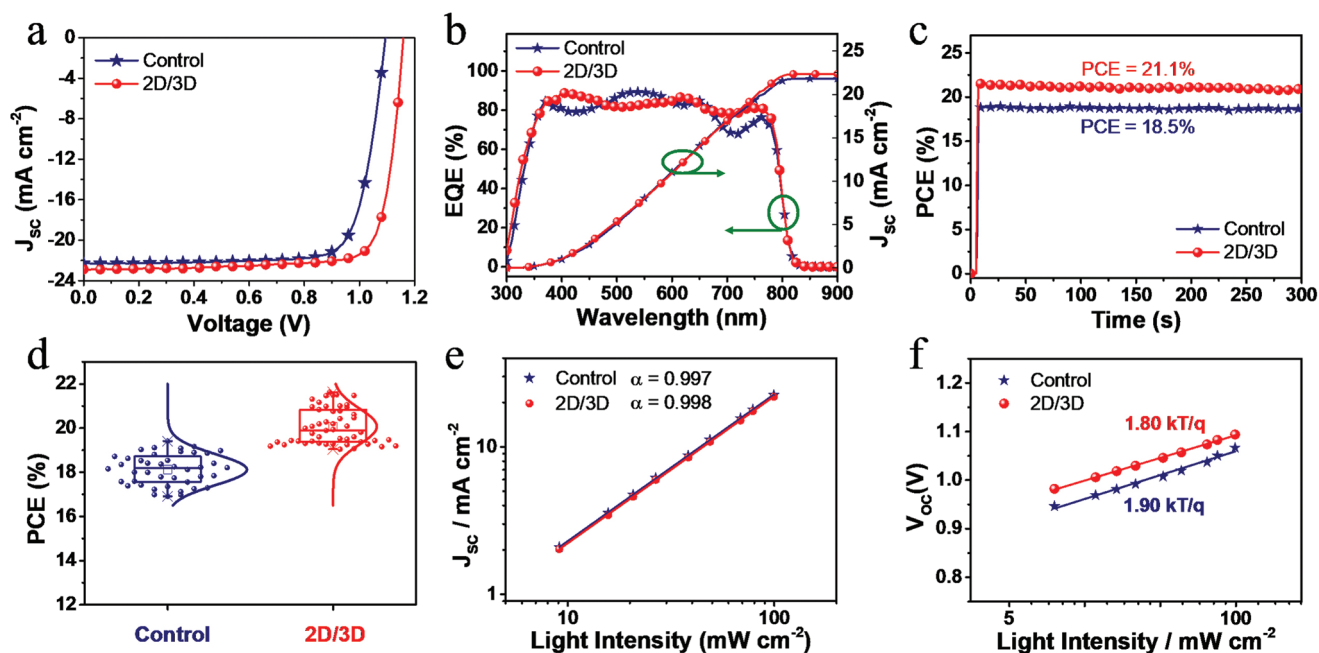
Figure 3. a) J–V curve of control and 2D/3D perovskite solar cells. b) EQE spectrum of the coressponding photovoltaic devices. c) Steady-state power output of the photovoltaic devices. d) The PCE distribution of control and 2D/3D perovskite devices. e) J_{SC} values of the photovoltaic devices versus light intensity on a double-logarithmic scale. f) V_{OC} values of the photovoltaic devices versus light intensity on a seminatural logarithmic scale.

and optimized 2D/3D perovskite solar cells under simulated AM1.5G irradiation (100 mW cm^{-2}). The control device showed an overall PCE of 19.16% with an open-current voltage (V_{OC}) of 1.09 V, a short-circuit current (J_{SC}) of 22.30 mA cm^{-2}, and a FF of 78.82%. Remarkably, a significant improved performance was obtained for the 2D/3D perovskite solar cells, achieving a large V_{OC} of 1.16 V, a J_{SC} of 22.8 mA cm^{-2}, and a very notable FF of 81.0%, resulting an impressive PCE of 21.49%. This efficiency is among the highest reported value so far for 2D/3D hybrid planar perovskite solar cells. The improvements in both V_{OC} and FF can be explained by improved crystallinity as evidenced by the SEM images and XRD results above. Moreover, the enhanced charge carrier lifetime and reduced nonradiative recombination for 2D/3D perovskite should contribute to the observed increase in V_{OC} and FF as discussed below. High crystallinity and preferred orientation will influence charge dissociation, transport, and diffusion length considerably.[48] Note that the electron-rich thiophene based ThMA is expected to provide better charge transport property in comparison with previously used insulating molecule such as butyl amine or benzene-based amine.[24] An initial test (Figure S7a; Table S2, Supporting Information) shows that the surface modification of control 3D perovskite using ThMAI could improve its photovoltaic performance, which may be ascribed to the better charge transport of ThMA cations or surface passivation effect or both, and will be further studied in our future work. Figure 3b shows the corresponding external quantum efficiency (EQE) spectra for the two photovoltaic devices. The integrated current densities are 21.82 and 22.36 mA cm^{-2}, respectively, in good agreement with the J_{SC} obtained from the J–V characteristics (**Table 1**). Nevertheless, the EQE exhibited very interesting features over the spectral response range of the device. Namely, the EQE value of 2D/3D perovskite device is higher at longer wavelengths at 600–800 nm, most likely from its improved and balanced charge carrier mobility and thus reduced carrier recombination discussed below. Note that the 2D/3D perovskite devices show reduced hysteresis in the J–V curves in comparison with that of control device (Figure S7b; Table S2, Supporting Information). The results indicate that the incorporation of ThMAI in the perovskite film could partially suppress the hysteresis, as the large ThMA organic cations cannot motion like small MA or FA cations, and it could also hinder the ions motion in perovskite film.[20] The steady-state power output of the devices measured at the maximum power point are shown in Figure 3c. After illuminating under 1 sun for 300 s, the cells exhibit a steady-state efficiency of 18.5% for the control device and 21.1% for 2D/3D hybrid perovskite device and in good agreement with the J–V measurements, indicating good stability of the devices. It was also found that the control devices showed poor transit stability, while the 2D/3D perovskite devices showed good transit stability

(Figure S8; Tables S3 and S4, Supporting Information) as well as good reproducibility (Figure 3d). These results can be explained by the reduced grain boundary shown in SEM images and the hindered ion motion resulted from the inserted large organic ThMA cations.

To further look into the charge transport property of control and 2D/3D perovskite films, a device structure of glass/ITO/poly(3,4-ethylenedioxythiophene) polystyrene sulfonate (PEDOT:PSS)/perovskite/spiro-OMeTAD/MoO$_3$/Ag was built up as hole-only devices, and glass/ITO/SnO$_2$/perovskite/[6,6]-phenyl-C61-butyric acid methyl ester (PCBM)/Bathocuproine (BCP)/Ag as electron-only device. The J–V characteristics of hole-only and electron-only devices are shown in Figure S9 and Table S5 (Supporting Information). By fitting the J–V curves to the space charge limited current (SCLC) model, the calculated hole mobility was 6.86×10^{-4} cm^2 V^{-1} s^{-1}, and the electron mobility was 1.28×10^{-3} cm^2 V^{-1} s^{-1} for the control perovskite film. But the 2D/3D hybrid perovskite exhibits more balanced hole and electron mobility of 2.09×10^{-3} and 2.14×10^{-3} cm^2 V^{-1} s^{-1}, respectively, resulting in higher FF of the photovoltaic device. The increased mobility is consistent with literature report,[49] and it may be ascribed to the enhanced grain size and improved crystallinity as well as crystalline orientation of perovskite in the film. These results further indicated that charge mobility could be improved when suitable amount large ThMA organic cations were incorporated into 3D perovskite and form the 2D/3D hybrid perovskite.

To understand the charge carrier recombination mechanism in 2D/3D hybrid perovskite, the power law dependence of the J_{SC} with light intensity ($J \propto I^\alpha$) was measured under light intensities ranging from 9 to 100 mW cm^{-2}. The control device was also measured for comparison. J_{SC} versus light intensity exhibits a linear relation in double-logarithmic scale, as shown in Figure 3e. The fitted α values of 2D/3D hybrid perovskite and the control devices are very close to 1, indicating negligible bimolecular recombination and no space charge effects for both devices,[50,51] which may be ascribed to the high quality perovskite films with low grain boundary defects. Figure 3f shows the seminatural logarithmic plot of V_{OC} as a function of light intensity for the devices and the slopes derived from the lines fitted linearly to the data. The control device exhibits a strong dependence of V_{OC} on the light intensity, with a slope of 1.9 kT/q, where k is Boltzmann's constant, q is the elementary charge, and T is the absolute temperature. The device based on 2D/3D perovskite exhibits a lower slope of 1.80 kT/q, indicating reduced trap-assisted Schockley–Read–Hall recombination in the device, which is ascribed to the enhanced crystallinity of 2D/3D perovskite film with reduced trap sites as well as the hindered ion motion due to the incorporation of large ThMA organic cations.[22]

Table 1. Optimized device parameters for the control and 2D/3D perovskites based devices.

	V_{OC} [V]	J_{SC} [mA cm^{-2}]	Integrated J_{SC} [mA cm^{-2}]	FF [%]	PCE [%]	μ_e [cm^2 V^{-1} s^{-1}]	μ_h [cm^2 V^{-1} s^{-1}]	μ_e/μ_h	Decay time[a] [µs]	Decay time[b] [µs]
Control	1.09	22.30	21.82	78.82	19.16	1.28×10^{-3}	6.86×10^{-4}	1.87	1.21	21.47
2D/3D	1.16	22.88	22.36	81.00	21.49	2.14×10^{-3}	2.09×10^{-3}	1.02	1.85	40.87

[a]Decay time extracted from TPL; [b]Decay time extracted from TPV.
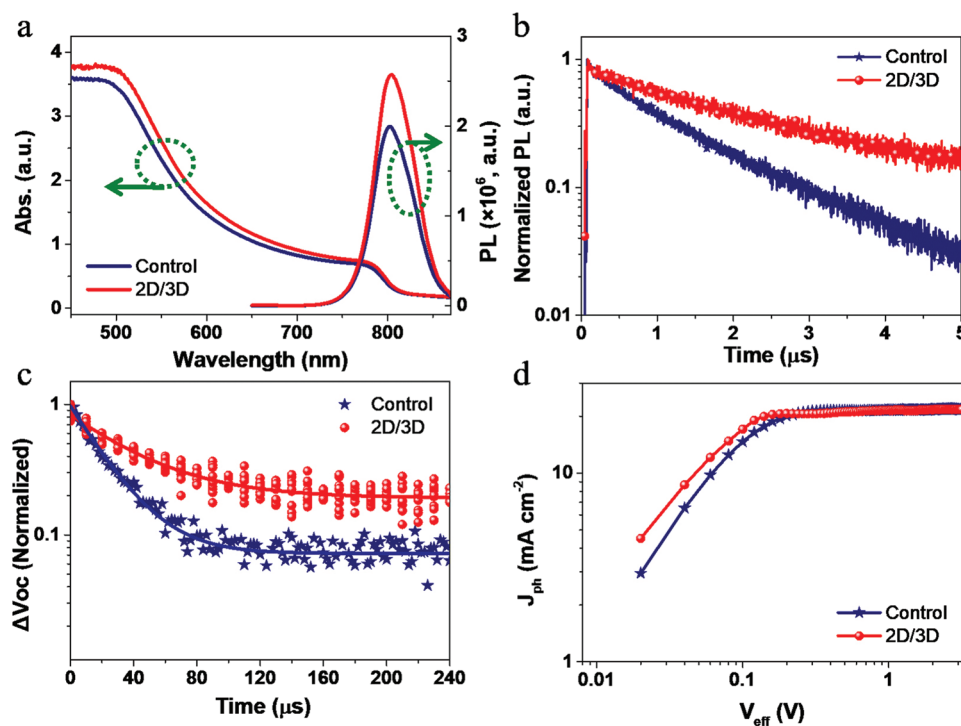
Figure 4. a) Absorption and steady-state PL spectra of control and 2D/3D perovskite films. b) Time-resolved photoluminescence spectra of control and 2D/3D perovskite films. c) Transient photovoltage (TPV) decay curves of the perovskite solar cells based on control and 2D/3D perovskites. d) Characteristics of photocurrent density versus effective voltage (J_{ph}–V_{eff}) on a double-logarithmic scale.

The absorption spectra of 2D/3D hybrid perovskite thin films showed very similar bandgap and absorption profiles in comparison with that of control 3D perovskite film, as illustrated in **Figure 4**a. These similar optical bandgaps were consistent with the onset photocurrent response in EQE curves shown above, indicating the negligible effect of a small fraction of large organic cations on the bandgap of the perovskite film.[35,42,52,53] Interestingly, the absorption intensity increased slightly over the entire region for 2D/3D perovskite film, which may be ascribed to a reduction in light scattering due to a smoother and larger grained perovskite film with high quality as observed in atomic force microscopy (AFM) (Figure S10, Supporting Information) and SEM images.[35] To compare the charge carrier dynamics of the control and 2D/3D perovskites in more details, we performed the steady-state photoluminescence (PL) and time-resolved photoluminescence (TPL) decay measurements. Compared with the control film, an increased PL intensity (Figure 4a) was observed for the 2D/3D hybrid film, which may be ascribed to its higher film quality with lower defect density. Note that the very slightly red-shifted PL peak may be due to the enhanced crystallinity or surface trap states of the 2D/3D perovskite film and will be further studied in our future work.[54] As demonstrated previously, the carrier dynamics derived from the TPL behavior provides information of trap-assisted charge recombination via nonradiative recombination related to the defect concentration.[55] As shown in Figure 4b, the 2D/3D perovskite film exhibits an increased carrier lifetime as compared to that of control perovskite film. The carrier lifetime of the control film was 1.21 µs, and the carrier lifetime was increased to 1.85 µs for 2D/3D film. The longer lifetime

of the PL transition in the 2D/3D hybrid film can be explained by the suppressed defect-induced nonradiative recombination due to the increase in crystallinity and the decrease in the concentration of defects, leading to improved V_{OC} and FF as measured from the J–V characteristics. This slower recombination, derived from the lower defect concentration, should involve an increase in V_{OC} due to efficient charge collection. Indeed, the average V_{OC} of the devices for 2D/3D hybrid perovskite was ≈1.11 V, which was larger than that (≈1.07 V) of control device (Figure 3d).

To find out how perovskite film affect the charge recombination process in the operating devices, transient photovoltage (TPV) measurement of the control and 2D/3D hybrid perovskite devices were conducted with light intensity of ≈0.5 sun, and laser pulses (532 nm, 10 ns) were applied to disturb the open circuited devices to trigger a small transient photovoltaic signal. As shown in Figure 4c, the photocurrent decay lifetimes are 21.47 and 40.87 µs for the control and 2D/3D perovskite devices, respectively. The longer delay time indicated the increased carrier lifetime and reduced charge carrier recombination rates in the 2D/3D perovskite device, which could be ascribed to the lower defect concentration in the film due to its good crystallinity as confirmed by SEM and XRD results discussed above. To further investigate the photoexcitation behavior of the fabricated devices, the photocurrent density (J_{ph}) versus effective voltage (V_{eff}) measurements were conducted. J_{ph} is determined by the equation $J_{ph} = J_L − J_D$, where J_L and J_D are the current densities measured under AM 1.5G illumination and in the dark, respectively. And V_{eff} is defined as $V_{eff} = V_0 − V_{app}$, where V_0 is the voltage when $J_{ph} = 0$ and V_{app}
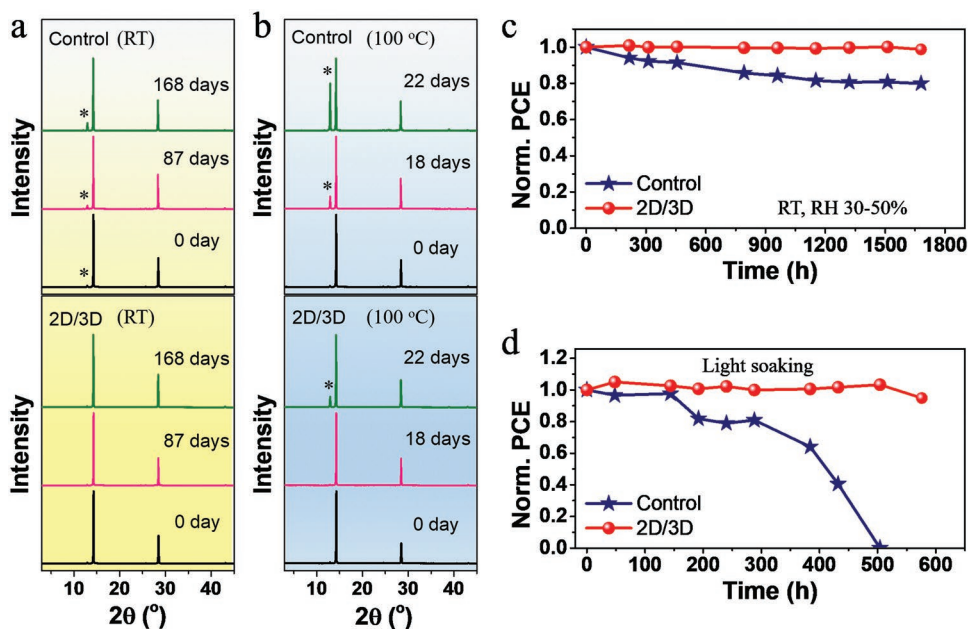
Figure 5. a) XRD patterns of control and 2D/3D perovskite films deposited on ITO/SnO$_2$ substrates exposed in ambient air with RH of 30–50%. b) XRD patterns of control and 2D/3D perovskite films deposited on ITO/SnO$_2$ substrates before and after exposed in ambient air at room temperature (RT). Asterisks denote the major reflections from PbI$_2$. c) Stability test of encapsulated devices in air with relative humidity (RH) of 30–50% at RT. d) Evolution of the PCEs measured from the unencapsulated devices exposed to continuous light soaking (100 mW cm^{-2}) in N$_2$.

is the applied bias. The ratio of J_{ph}/J_{sat} can be used to estimate the charge collection efficiency under operation conditions, where J_{sat} is the saturation photocurrent density.[56,57] Under short circuit conditions, the J_{ph}/J_{sat} ratios were calculated to be 0.958 and 0.991 for the control and 2D/3D perovskite devices, respectively. Under the maximal power output conditions, the J_{ph}/J_{sat} ratios were 0.916 for control device and 0.945 for 2D/3D perovskite device. The larger value of J_{ph}/J_{sat} indicates a better charge collection efficiency in 2D/3D perovskite device, consisting with the higher FF.

The longevity of perovskite devices has been attracted much attention due to the moisture-sensitive nature of metal halide perovskites. The increased hydrophobicity of 2D/3D perovskite discussed above would have the potential to protect the perovskite film from humidity, leading to improved film and device stability. Effects of direct exposure of the perovskite films to ambient conditions (air, 30–50% relative humidity (RH), room temperature (RT) in dark) were monitored for 168 days. As shown in **Figure 5**a, the aged control 3D perovskite film exhibits an obvious diffraction peak for PbI$_2$ at 12.9° due to the degradation of perovskite film. Importantly, no obvious changes were observed in the XRD patterns for 2D/3D perovskite film after 168 days. A heat test was further performed to validate the thermal stability of control and 2D/3D perovskite films at 100 °C in air (RH 40–50%). As shown in Figure 5b, a strong PbI$_2$ peak was observed for control perovskite film after 22 days, while only a small PbI$_2$ peak appeared in 2D/3D perovskite film. These results indicate that the ThMA-incorporated 2D/3D perovskite film exhibits excellent environment and thermal stability in comparison with that of control film, which could be ascribed to the improved hydrophobicity of thiophene units resulting from the incorporation of ThMA spacer cations as discussed above.

Considering the realistic application of solar cells, we investigated stability of encapsulated devices stored in ambient condition with a cover with relative humidity of 30–50%. Note that we employ Au to replace Ag as top electrode for this encapsulated device stability test. As shown in Figure 5c and Figure S11 (Supporting Information), the device employing 2D/3D perovskite shows greatly improved stability in comparison with that of the control device. The 2D/3D perovskite device retains over 99% of its initial PCE after 1680 h (over 66 days), whereas the control device decays to 80% of the original performance. Enhanced stability under ambient condition is likely to be attributed to better intrinsic material stability as discussed above. These results are consistent with the measured stability data for devices stored in N$_2$, where the 2D/3D perovskite device maintained 92% of their initial PCE after 2500 h (over 100 days), while the control device only retained 62% of their initial efficiency (Figure S12, Supporting Information). Importantly, the thermal stability of 2D/3D perovskite devices (70 °C) in N$_2$ were also dramatically improved (Figure S13, Supporting Information), which is consistent with the heat test results of the films. We have further carried a near real environmental stability test with complete devices without encapsulation (the devices were exposed directly to the environment near the windows, without any cover) with relative humidity of 30–50%. The 2D/3D hybrid perovskite based device exhibits high stability by retaining 96% of the initial device performance after 220 h (Figure S14, Supporting Information), which demonstrates its robustness under ambient conditions in air. However, the control device revealed a fast degradation rate by losing more than 68% of the initial efficiency under the same condition.

Light illumination is known to be a critical intrinsic factor for stability of perovskite solar cells.[58] Figure 5d and Figure S15

(Supporting Information) shows the light exposure test of the devices stored in N_2 glove box under continuous light illumination (white light-emitting diode (LED), 100 mW cm^{-2}). We observed that the efficiency of control device was dramatically decreased to 0 after 500 h, while the 2D/3D hybrid perovskite devices still maintained over 94% of its original efficiency after 576 h, showing less than 6% decrease, indicating the enhanced long-term stability of 2D/3D perovskite devices. The improved stability is consistent with the beneficial effect on the active layer stability of ThMA-incorporated 2D/3D perovskite film discussed above. Overall, the enhanced crystallinity, the reduced crystal defect and the suppressed ion motion account for superior stability of 2D/3D hybrid perovskite in the planar photovoltaic devices. Together with the simplicity and scalability of our new approach, the significantly improved stability as well as high efficiency indicate the great potential of ThMAI based 2D/3D hybrid perovskite solar cells for industrial applications.

In conclusion, we have demonstrated that the ThMA spacer cations can be successfully embedded into the FAI and MAI based 3D perovskite and induce the crystalline growth and orientation of the obtained 2D/3D hybrid perovskite. The incorporation of ThMA spacer cation for 2D/3D hybrid perovskite enlarges the perovskite grain size, lengthens the carrier lifetime, and suppresses the charge carrier recombination, leading to significantly improved efficiency and stability of the devices. The highest PCE of 21.49% was achieved for photovoltaic device based on the 2D/3D hybrid perovskite, combined with a high V_{OC} of 1.16 V and a notable FF of 81%. Furthermore, the 2D/3D hybrid perovskite films show greatly improved stability due to the improved hydrophobic property of perovskite film and the suppressed ion migration because of the incorporation of large ThMA spacer cations. For example, the encapsulated 2D/3D hybrid perovskite-based devices retained over 99% of their initial photovoltaic performance after storage 1680 h in air, compared to 80% initial performance left for the control device. In addition, the device stability under continuous light soaking (100 mW cm^{-2}) was enhanced significantly for 2D/3D perovskite device in comparison with control device. These results demonstrate that the incorporation of a small fraction of ThMA spacer cations into 3D perovskite forming 2D/3D hybrid materials could induce the crystalline growth and orientation and is an efficient strategy to combine the advantage of 2D and 3D perovskite toward stable and efficient solar cells for future industry application.

Experimental Section

Device Fabrication: The planner perovskite solar cells were fabricated on ITO substrates. ITO glasses were sequentially cleaned with distilled water, acetone and isopropyl alcohol. The as-cleaned thin layer of SnO_2 colloid precursor was spin-coated onto the ITO surface at 3000 rpm for 30 s in ambient air, and then heated on a hot plate in ambient air at 150 °C for 30 min. After cooling to room temperature, the substrate was treated with UV-ozone for 8 min before spin coating of perovskite solution. The coated substrates were then transferred to a glovebox filled with nitrogen. Typically, PbI_2 was dissolved in DMF at a concentration of 1.0 M, followed by stirred at 70 °C for 12 h. Then the PbI_2 solution was deposited by spin coating at 2000 rpm for 30 s, and then annealed at 70 °C for 15 min. After cooling down to room temperature, a solution of FAI:MAI:MACl (weight ratio, 51:9:12; 72 mg mL^{-1} in total, in isopropanol) with different content of ThMAI was spin-coated on the top of the PbI_2 layer at 3000 rpm for 40 s, followed with thermal annealing at 140 °C for 20 min in air (relative humidity ≈ 40%). The optimized ThMAI content for 2D/3D perovskite is 8% of the total weight of FAI and MAI. The HTL solution was then deposited by spin coating at 6000 rpm for 30 s. The HTL solution was prepared by dissolving 80 mg of Spiro-OMeTAD, 30 µL of 4-*tert*-butylpyridine, and 35 µL of lithium bis(trifluoromethylsulfonyl)-imide (260 mg mL^{-1} in acetonitrile) in 1 mL chlorobenzene. The as deposited samples aged under dry air condition for ≈12 h. Finally, a 15 nm MoO_3 layer and 80 nm Ag layer were deposited by thermal evaporation under a pressure of 1.0×10^{-4} Pa. The effective area was 10 mm^2 defined by mask.

Supporting Information

Supporting Information is available from the Wiley Online Library or from the author.

Acknowledgements

Conflict of Interest

The authors declare no conflict of interest.

Keywords

[1] J. P. Correa-Baena, M. Saliba, T. Buonassisi, M. Gratzel, A. Abate, W. Tress, A. Hagfeldt, *Science* **2017**, *358*, 739.

[2] M. Gratzel, *Acc. Chem. Res.* **2017**, *50*, 487.

[3] M. A. Green, A. Ho-Baillie, H. J. Snaith, *Nat. Photonics* **2014**, *8*, 506.

[4] T. M. Brenner, D. A. Egger, L. Kronik, G. Hodes, D. Cahen, *Nat. Rev. Mater.* **2016**, *1*, 15007.

[5] G. E. Eperon, M. T. Horantner, H. J. Snaith, *Nat. Rev. Chem.* **2017**, *1*, 0095.

[6] J. Berry, T. Buonassisi, D. A. Egger, G. Hodes, L. Kronik, Y. L. Loo, I. Lubomirsky, S. R. Marder, Y. Mastai, J. S. Miller, D. B. Mitzi, Y. Paz, A. M. Rappe, I. Riess, B. Rybtchinski, O. Stafsudd, V. Stevanovic, M. F. Toney, D. Zitoun, A. Kahn, D. Ginley, D. Cahen, *Adv. Mater.* **2015**, *27*, 5102.

[7] A. Kojima, K. Teshima, Y. Shirai, T. Miyasaka, *J. Am. Chem. Soc.* **2009**, *131*, 6050.

[8] H. S. Kim, C. R. Lee, J. H. Im, K. B. Lee, T. Moehl, A. Marchioro, S. J. Moon, R. Humphry-Baker, J. H. Yum, J. E. Moser, M. Gratzel, N. G. Park, *Sci. Rep.* **2012**, *2*, 591.

[9] H. P. Zhou, Q. Chen, G. Li, S. Luo, T. B. Song, H. S. Duan, Z. R. Hong, J. B. You, Y. S. Liu, Y. Yang, *Science* **2014**, *345*, 542.

[10] W. S. Yang, B. W. Park, E. H. Jung, N. J. Jeon, Y. C. Kim, D. U. Lee, S. S. Shin, J. Seo, E. K. Kim, J. H. Noh, S. I. Seok, *Science* **2017**, *356*, 1376.

[11] National Renewable Energy Laboratory Efficiency Chart, https://www.nrel.gov/pv/assets/pdfs/pv-efficiency-chart.20190103.pdf (accessed: February 2019).

[12] H. R. Tan, A. Jain, O. Voznyy, X. Z. Lan, F. P. G. de Arquer, J. Z. Fan, R. Quintero-Bermudez, M. J. Yuan, B. Zhang, Y. C. Zhao, F. J. Fan, P. C. Li, L. N. Quan, Y. B. Zhao, Z. H. Lu, Z. Y. Yang, S. Hoogland, E. H. Sargent, *Science* **2017**, *355*, 722.

[13] Y. Hou, X. Y. Du, S. Scheiner, D. P. McMeekin, Z. P. Wang, N. Li, M. S. Killian, H. W. Chen, M. Richter, I. Levchuk, N. Schrenker, E. Spiecker, T. Stubhan, N. A. Luechinger, A. Hirsch, P. Schmuki, H. P. Steinruck, R. H. Fink, M. Halik, H. J. Snaith, C. J. Brabec, *Science* **2017**, *358*, 1192.

[14] H. Chen, F. Ye, W. T. Tang, J. J. He, M. S. Yin, Y. B. Wang, F. X. Xie, E. B. Bi, X. D. Yang, M. Gratzel, L. Y. Han, *Nature* **2017**, *550*, 92.

[15] Z. Wang, Z. J. Shi, T. T. Li, Y. H. Chen, W. Huang, *Angew. Chem., Int. Ed.* **2017**, *56*, 1190.

[16] N. G. Park, M. Gratzel, T. Miyasaka, K. Zhu, K. Emery, *Nat. Energy* **2016**, *1*, 16152.

[17] Y. G. Rong, L. F. Liu, A. Y. Mei, X. Li, H. W. Han, *Adv. Energy Mater.* **2015**, *5*, 1501066.

[18] W. S. Yang, J. H. Noh, N. J. Jeon, Y. C. Kim, S. Ryu, J. Seo, S. I. Seok, *Science* **2015**, *348*, 1234.

[19] D. J. Kubicki, D. Prochowicz, A. Hofstetter, S. M. Zakeeruddin, M. Gratzel, L. Emsley, *J. Am. Chem. Soc.* **2017**, *139*, 14173.

[20] T. Singh, T. Miyasaka, *Adv. Energy Mater.* **2018**, *8*, 1700677.

[21] B. W. Park, S. I. Seok, *Adv. Mater.* **2019**, 1805337.

[22] J. Chen, D. Lee, N. G. Park, *ACS Appl. Mater. Interfaces* **2017**, *9*, 36338.

[23] H. H. Tsai, W. Y. Nie, J. C. Blancon, C. C. S. Toumpos, R. Asadpour, B. Harutyunyan, A. J. Neukirch, R. Verduzco, J. J. Crochet, S. Tretiak, L. Pedesseau, J. Even, M. A. Alam, G. Gupta, J. Lou, P. M. Ajayan, M. J. Bedzyk, M. G. Kanatzidis, A. D. Mohite, *Nature* **2016**, *536*, 312.

[24] Y. N. Chen, Y. Sun, J. J. Peng, J. H. Tang, K. B. Zheng, Z. Q. Liang, *Adv. Mater.* **2018**, *30*, 1703487.

[25] X. H. Zhu, N. Mercier, A. Riou, P. Blanchard, P. Frere, *Chem. Commun.* **2002**, *0*, 2160.

[26] A. H. Proppe, R. Quintero-Bermudez, H. R. Tan, O. Voznyy, S. O. Kelley, E. H. Sargent, *J. Am. Chem. Soc.* **2018**, *140*, 2890.

[27] J. X. Liu, J. Leng, K. F. Wu, J. Zhang, S. Y. Jin, *J. Am. Chem. Soc.* **2017**, *139*, 1432.

[28] X. Zhang, X. D. Ren, B. Liu, R. Munir, X. J. Zhu, D. Yang, J. B. Li, Y. C. Liu, D. M. Smilgies, R. P. Li, Z. Yang, T. Q. Niu, X. L. Wang, A. Amassian, K. Zhao, S. Z. F. Liu, *Energy Environ. Sci.* **2017**, *10*, 2095.

[29] C. Q. Ma, D. Shen, T. W. Ng, M. F. Lo, C. S. Lee, *Adv. Mater.* **2018**, *30*, 1800710.

[30] H. T. Lai, B. Kan, T. T. Liu, N. Zheng, Z. Q. Xie, T. Zhou, X. J. Wan, X. D. Zhang, Y. S. Liu, Y. S. Chen, *J. Am. Chem. Soc.* **2018**, *140*, 11639.

[31] R. Yang, R. Z. Li, Y. Cao, Y. Q. Wei, Y. F. Miao, W. L. Tan, X. C. Jiao, H. Chen, L. D. Zhang, Q. Chen, H. T. Zhang, W. Zou, Y. M. Wang, M. Yang, C. Yi, N. N. Wang, F. Gao, C. R. McNeill, T. S. Qin, J. P. Wang, W. Huang, *Adv. Mater.* **2018**, *30*, 1804771.

[32] W. F. Fu, J. Wang, L. J. Zuo, K. Gao, F. Liu, D. S. Ginger, A. K. Y. Jen, *ACS Energy Lett.* **2018**, *3*, 2086.

[33] N. Zhou, Y. H. Shen, L. Li, S. Q. Tan, N. Liu, G. H. J. Zheng, Q. Chen, H. P. Zhou, *J. Am. Chem. Soc.* **2018**, *140*, 459.

[34] H. Y. Zheng, G. Z. Liu, L. Z. Zhu, J. J. Ye, X. H. Zhang, A. Alsaedi, T. Hayat, X. Pan, S. Y. Dai, *Adv. Energy Mater.* **2018**, *8*, 1800051.

[35] Z. F. Wu, S. R. Raga, E. J. Juarez-Perez, X. Y. Yao, Y. Jiang, L. K. Ono, Z. J. Ning, H. Tian, Y. B. Qi, *Adv. Mater.* **2018**, *30*, 1703670.

[36] J. F. Lu, L. C. Jiang, W. Li, F. Li, N. K. Pai, A. D. Scully, C. M. Tsai, U. Bach, A. N. Simonov, Y. B. Cheng, L. Spiccia, *Adv. Energy Mater.* **2017**, *7*, 1700444.

[37] Y. Hu, Z. H. Zhang, A. Y. Mei, Y. Y. Jiang, X. M. Hou, Q. F. Wang, K. Du, Y. G. Rong, Y. H. Zhou, G. Z. Xu, H. W. Han, *Adv. Mater.* **2018**, *30*, 1705786.

[38] G. Grancini, C. Roldan-Carmona, I. Zimmermann, E. Mosconi, X. Lee, D. Martineau, S. Narbey, F. Oswald, F. De Angelis, M. Graetzel, M. K. Nazeeruddin, *Nat. Commun.* **2017**, *8*, 15684.

[39] J. W. Lee, Z. H. Dai, T. H. Han, C. Choi, S. Y. Chang, S. J. Lee, N. De Marco, H. X. Zhao, P. Y. Sun, Y. Huang, Y. Yang, *Nat. Commun.* **2018**, *9*, 3021.

[40] A. D. Jodlowski, C. Roldan-Carmona, G. Grancini, M. Salado, M. Ralaiarisoa, S. Ahmad, N. Koch, L. Camacho, G. de Miguel, M. K. Nazeeruddin, *Nat. Energy* **2017**, *2*, 972.

[41] T. M. Koh, V. Shanmugam, J. Schlipf, L. Oesinghaus, P. Muller-Buschbaum, N. Ramakrishnan, V. Swamy, N. Mathews, P. P. Boix, S. G. Mhaisalkar, *Adv. Mater.* **2016**, *28*, 3653.

[42] D. H. Cao, C. C. Stoumpos, O. K. Farha, J. T. Hupp, M. G. Kanatzidis, *J. Am. Chem. Soc.* **2015**, *137*, 7843.

[43] Q. Jiang, Z. N. Chu, P. Y. Wang, X. L. Yang, H. Liu, Y. Wang, Z. G. Yin, J. L. Wu, X. W. Zhang, J. B. You, *Adv. Mater.* **2017**, *29*, 1703852.

[44] Y. C. Kim, N. J. Jeon, J. H. Noh, W. S. Yang, J. Seo, J. S. Yun, A. Ho-Baillie, S. J. Huang, M. A. Green, J. Seidel, T. K. Ahn, S. I. Seok, *Adv. Energy Mater.* **2016**, *6*, 1502104.

[45] Q. Chen, H. P. Zhou, T. B. Song, S. Luo, Z. R. Hong, H. S. Duan, L. T. Dou, Y. S. Liu, Y. Yang, *Nano Lett.* **2014**, *14*, 4158.

[46] D. B. Mitzi, *J. Chem. Soc., Dalton Trans.* **2001**, 1.

[47] Z. Y. Cheng, J. Lin, *CrystEngComm* **2010**, *12*, 2646.

[48] J. M. Ball, A. Petrozza, *Nat. Energy* **2016**, *1*, 1.

[49] P. W. Li, Y. Q. Zhang, G. Liang, G. C. Xing, X. L. Liu, F. Y. Li, X. T. Liu, X. T. Hu, G. S. Shao, Y. L. Song, *Adv. Mater.* **2018**, 1805323.

[50] V. D. Mihailetchi, J. Wildeman, P. W. Blom, *Phys. Rev. Lett.* **2005**, *94*, 126602.

[51] D. Bi, L. Yang, G. Boschloo, A. Hagfeldt, E. M. Johansson, *J. Phys. Chem. Lett.* **2013**, *4*, 1532.

[52] B.-E. Cohen, M. Wierzbowska, L. Etgar, *Adv. Funct. Mater.* **2017**, *27*, 1604733.

[53] J. Xing, Y. B. Zhao, M. Askerka, L. N. Quan, X. W. Gong, W. J. Zhao, J. X. Zhao, H. R. Tan, G. K. Long, L. Gao, Z. Y. Yang, O. Voznyy, J. Tang, Z. H. Lu, Q. H. Xiong, E. H. Sargent, *Nat. Commun.* **2018**, *9*, 3541.

[54] Y. H. Shao, Z. G. Xiao, C. Bi, Y. B. Yuan, J. S. Huang, *Nat. Commun.* **2014**, *5*, 5784.

[55] N. K. Noel, A. Abate, S. D. Stranks, E. S. Parrott, V. M. Burlakov, A. Goriely, H. J. Snaith, *ACS Nano* **2014**, *8*, 9815.

[56] Y. W. Wang, B. Wu, Z. H. Wu, Z. J. Lan, Y. F. Li, M. J. Zhang, F. R. Zhu, *J. Phys. Chem. Lett.* **2017**, *8*, 5264.

[57] G. Y. Xu, P. Q. Bi, S. H. Wang, R. M. Xue, J. W. Zhang, H. Y. Chen, W. J. Chen, X. T. Hao, Y. W. Li, Y. F. Li, *Adv. Funct. Mater.* **2018**, *28*, 1804427.

[58] K. Domanski, E. A. Alharbi, A. Hagfeldt, M. Gratzel, W. Tress, *Nat. Energy* **2018**, *3*, 61.